

A statistical investigation of the effects of grain boundary properties on transgranular fracture

R.H. Kraft^a, J.F. Molinari^{b,*}

^a Department of Mechanical Engineering, The Johns Hopkins University, 104 Latrobe Hall, 3400 North Charles Street, Baltimore, MD 21218, USA

^b LSMS, IS, ENAC, Ecole Polytechnique Fédérale de Lausanne (EPFL), CH-1015 Lausanne, Switzerland

Received 20 November 2007; received in revised form 14 May 2008; accepted 14 May 2008

Available online 5 July 2008

Abstract

A two-dimensional finite-element model is developed to investigate transgranular fracture in polycrystalline alumina under tensile loading. Microcracking is modeled explicitly using the cohesive interface approach. The effects of grain boundary distributions on mesoscopic failure strength and fracture energy, and the resulting percentages of transgranular fracture are examined. Results are based on 20 different realizations of microstructures in an attempt to capture the stochastic nature of brittle failure. Numerical results indicate that the grain boundary distribution has profound effects on mesoscopically observed values, which are in part controlled by the crack propagation path. Based on observations of the simulated crack path, microstructural engineering with respect to grain morphology is conducted, leading to a significant increase in performance.

© 2008 Acta Materialia Inc. Published by Elsevier Ltd. All rights reserved.

Keywords: Ceramic material; Fracture mechanisms; Transgranular fracture; Microstructures; Cohesive interface

1. Introduction

A firm understanding of the underlying mechanisms of brittle fracture is of scientific and practical importance because these mechanisms determine a materials' fracture toughness and strength. Two such mechanisms are inter- and transgranular fracture. Both mechanisms have been observed in polycrystalline aluminum oxide (Al_2O_3) and have been documented at various levels of detail [see e.g. 1–3]. The ability to uncover and model the relationship between microstructural properties (such as grain size), percentages of inter- and transgranular fracture, and the resulting fracture toughness and strength may lead to the design of materials with improved performance.

For brittle ceramics such as Al_2O_3 , a propagating crack will travel along the grain boundary or through the grain depending on the crack incident angle and the ratio of

the grain boundary fracture energy, E_{GB} , to the surface energy of crystal planes, E_{G} [4,5]. The ratio $E_{\text{GB}}/E_{\text{G}}$ is a function of material chemistry and processing, and can strongly affect observed behavior. The previous literature can sometimes seem contradictory without full knowledge of the microstructural characteristics. For example, Gutshall and Gross [1] examined fracture in polycrystalline Al_2O_3 and found that a combination of inter- and transgranular fracture was observed in all specimens fractured at room temperature. Fracture energy (and per cent of transgranular fracture) increased with increasing grain size. However, Simpson [6], also studying polycrystalline alumina, observed that the fracture energy decreased as grain size increased. Simpson postulated that the opposing results were due to the lack of transgranular fracture caused by weak, porous grain boundaries that allowed intergranular fracture to be the dominating mechanism at all grain sizes. An interesting observation can be made from these examples. In the latter study, a much more tortuous crack path for larger grain sizes might be expected, resulting therefore in higher fracture energy. But this was

* Corresponding author. Tel.: +41 1 21 693 24 11.

E-mail address: jean-francois.molinari@epfl.ch (J.F. Molinari).

not found to be the case because the grain boundaries were weak. Thus, a tortuous crack path may not lead to higher fracture energy; ultimately it depends on the material properties as well. These findings raise an important question: what is the optimum ratio of E_{GB}/E_G that allows high fracture toughness without compromising strength?

Various approaches, both analytic and computational, have been taken to model transgranular fracture. Analytic statistical approaches which include cleavage fracture have been able to capture the statistical variations of fracture toughness and strength as functions of mechanical properties and microstructural characteristics, such as yield stress and grain size, over a range of temperatures [7,8]. One important conclusion drawn from these analyses is that it is extremely important to base any statistical analysis of data on a good micromechanistic model. Energetic theoretical models have shown great promise as a means to achieve-controlled fracture paths to balance inter- and transgranular fracture for desired mechanical performance. For example, preferred orientation and grain geometry (such as elongation) can have profound effects on the percentages of transgranular fracture and the resulting fracture energy [9–11]. Insightful research has been conducted which combines experimental observations and finite-element modeling with the goal of examining effects of residual stresses caused by thermal loading and processing on Al_2O_3 microcracking [12–14]. Realistic microstructures could adequately represent stress inhomogeneities; however, microcracking was not captured explicitly, but instead through mutation of the stiffness tensor. Recently, finite-element-based micromechanical modeling has contributed to our understanding of damage evolution in brittle materials [15–19]. However, to the authors' knowledge, there has been no finite-element modeling of transgranular fracture where cracking was captured explicitly using cohesive interfaces.

In the hope of contributing to the understanding of what controls the strength and fracture characteristics of ceramics, eventually leading to improved design of microstructures, we have developed a computational tool to simulate transgranular fracture. Specifically, we hope to shed light on the effects of different types of distributions on the percentages of inter- and transgranular fracture, and how, in turn, the mesoscopic fracture toughness and strength is affected. There are numerous advantages to using computations in this sort of problem. For example, as Simpson [6] concludes, completely stable crack propagation is required to study microstructural effects on fracture energy, which can be a difficult to maintain in a experimental laboratory setting, yet this is easier to do using computations.

2. Numerical framework

2.1. Finite-element method

The finite-element method was used in the Lagrangian framework. The equation of motion was discretized using

a second-order explicit time scheme and standard six-node triangles were used to discretize space [20]. The interactions of grains in the simulation are considered using a small strain multibody interface algorithm that computes contact, adhesion and frictional forces. This algorithm has recently been used to study compressive loading of brittle materials [17,19]. The interaction between grain boundary junctions was handled by considering pairs of contacting grains, so at a triple junction there are three pairs of grains. The contact algorithm loops through pairs of grains, which allows multiple junctions to be considered. However, the algorithm loses accuracy due to interpenetration of the last contact pair but this is negligible because of the small time step (on the order of picoseconds).

2.2. Contact

For contact, a two-step procedure was used [21]. The unconstrained kinematic variables were predicted first, then corrected to account for contact, adhesion and friction between grains. The predicted acceleration $\mathbf{a}_i^{\text{pred}}$, velocity $\mathbf{v}_i^{\text{pred}}$ and displacement $\mathbf{d}_i^{\text{pred}}$ vectors of a given node i are:

$$\mathbf{a}_i^{\text{pred}} = \frac{\mathbf{f}_i^n}{m_i} \quad (1)$$

$$\mathbf{v}_i^{\text{pred}} = \mathbf{v}_i^n + \mathbf{a}_i^n \Delta t \quad (2)$$

$$\mathbf{d}_i^{\text{pred}} = \mathbf{d}_i^n + \mathbf{v}_i^{\text{pred}} \Delta t \quad (3)$$

where m_i is the lumped mass of node i , \mathbf{f}_i^n is the residual force vector calculated at the element level, Δt is the time step, and \mathbf{d}_i^n , \mathbf{v}_i^n , and \mathbf{a}_i^n are the current displacements, velocities and accelerations. The corrected acceleration $\mathbf{a}_i^{\text{corr}}$, velocity $\mathbf{v}_i^{\text{corr}}$ and displacement $\mathbf{d}_i^{\text{corr}}$ vectors are computed based on a corrective force calculated from the predicted, unconstrained displacements, $\mathbf{d}_i^{\text{pred}}$. In the case of interpenetration of a node i into a surface defined by nodes j and k , the correction force, $\mathbf{f}_i^{\text{corr}}$ [17] is:

$$\mathbf{f}_i^{\text{corr}} = \frac{\delta_i}{2\Delta t^2(1/m_j + 1/m_k^s)} \quad (4)$$

where

$$m_i^s = \alpha m_j + (1 - \alpha) m_k \quad (5)$$

with α being a weighting factor between zero and one specifying the proximity of node i to node j on the contact surface. δ_i represents the shortest distance vector between node i and the contact surface. The factor of $\frac{1}{2}$ in Eq. (4) is because the subscript i implies a loop over all nodes and the factor allows a two-pass master–slave algorithm to be used. In order to preserve linear momentum, an opposing force is applied to the contact surface using nodes j and k :

$$\mathbf{f}_j^{\text{corr}} = -\alpha \mathbf{f}_i^{\text{corr}} \quad (6)$$

$$\mathbf{f}_k^{\text{corr}} = -(1 - \alpha) \mathbf{f}_i^{\text{corr}} \quad (7)$$

2.3. Adhesion and friction

For both tension and shear the separation of interfaces is controlled by a cohesive law [22,23]. For this, δ_i is decomposed into the normal and shearing components which are coupled through a parameter ξ , using the relation:

$$\delta_{\text{eff}} = \sqrt{\delta_n^2 + \xi \delta_s^2} \quad (8)$$

where δ_n and δ_s are the normal and shear opening displacements given by:

$$\delta_n = \delta_i \cdot \mathbf{n}_i \quad (9)$$

$$\delta_s = |\delta_i - \delta_n \mathbf{n}_i| \quad (10)$$

with \mathbf{n}_i the unit normal to the contact surface. The coupling parameter ξ assigns different weights to the sliding and normal opening displacements and is set equal to 0.7. In adhesion, $\mathbf{f}_i^{\text{corr}}$ becomes a tensile force across the interface of two adjacent grains. Once $\mathbf{f}_i^{\text{corr}}$ reaches a critical value, it gets adjusted according to a cohesive interface law and can be considered a nucleated microcrack. A reversible linear decreasing cohesive law is used for the behavior of the grain boundaries. The law is schematically represented in Fig. 1. The full material description is given by the parameters δ_c (the critical crack opening displacement) and σ_c (the tensile strength). These two values define the fracture energy release rate, G_c :

$$G_c = \frac{1}{2} \sigma_c \delta_c \quad (11)$$

The virtual crack becomes a fully open crack when $\delta_{\text{eff}} \geq \delta_c$. Once the crack has fully opened, friction is activated which resists motion tangential to the contacting surface, i.e.

$$f_f = \mu_f f_n \quad (12)$$

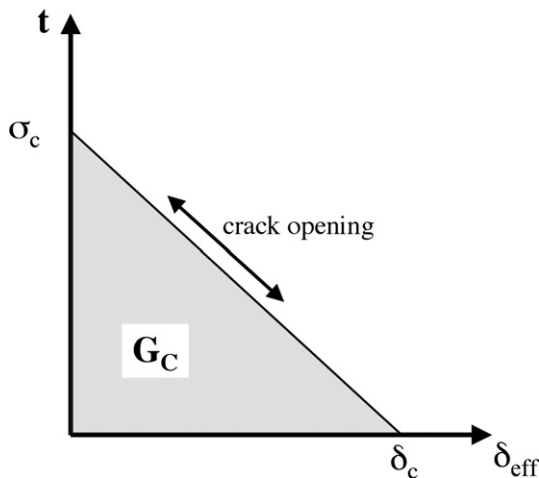


Fig. 1. Reversible cohesive law used in adhesion of the grain boundaries. Once the crack is open frictional forces that oppose tangential motion are prescribed.

where f_n is the resolved normal force on the surface.

In this approach, we construct the cohesive interface parameters, σ_c and δ_c , based on experimental data obtained from bicrystal experiments [24]. Another approach for obtaining cohesive properties would be to extract σ_c and δ_c from molecular dynamics simulations. In such an approach, attention must be given to the interatomic potential used in the molecular dynamics. For example, using two different interatomic potentials may yield different values of σ_c . There is a multitude of literature on this subject [see e.g. 25,26].

2.4. Modeling transgranular fracture

In order to model transgranular fracture an additional computational routine was developed to adaptively remesh and insert cohesive interfaces along hypothetical crystallographic directions. In real materials, fracture may occur along crystallographic planes which reside within the unit cell. Fracture may be more likely to occur on a given plane due to a combination of the resolved stress and the fracture toughness along that plane. In this paper we take this three-dimensional problem, and simplify it to two dimensions and allow only three available fracture planar directions per grain. Each plane has the same energy release rate, G_c , associated with it, and fracture strengths on each plane are assumed to be isotropic. One fracture plane orientation is randomly assigned per grain; then two more fracture planes are oriented 60° and 120° apart from the first random orientation.

Transgranular interfaces are dynamically inserted across a grain based on two criteria: the resolved normal and shear stresses, σ and τ , respectively. Remeshing is conducted if:

$$\sigma \geq \sigma_{\text{crit}} \quad (13)$$

or

$$\tau \geq \tau_{\text{crit}} \quad (14)$$

where σ_{crit} and τ_{crit} are the critical normal and shear stresses, respectively. These values are obtained from single-crystal experiments as described in a later section. The evaluation of the insertion criterion is schematically depicted in Fig. 2. During the simulation, the slip direction at each finite-element integration point is obtained by projecting the local deformation gradient, \mathbf{F} onto each of the grain orientations, \mathbf{v}_i , where i goes from 1 to 3:

$$\mathbf{r}_i = \frac{\mathbf{F} \mathbf{v}_i}{\|\mathbf{F} \mathbf{v}_i\|} \quad (15)$$

The resolved normal stress, σ_i , is given by:

$$\sigma_i = (\boldsymbol{\sigma} \mathbf{n}_i) \cdot \mathbf{n}_i \quad (16)$$

where \mathbf{n}_i is the normal to the slip plane ($\mathbf{n}_i \perp \mathbf{r}_i$) and $\boldsymbol{\sigma}$ is the local stress field at the integration point. The resolved shear stress, τ_i , is given by:

$$\tau_i = (\boldsymbol{\sigma} \mathbf{n}_i) \cdot \mathbf{r}_i \quad (17)$$

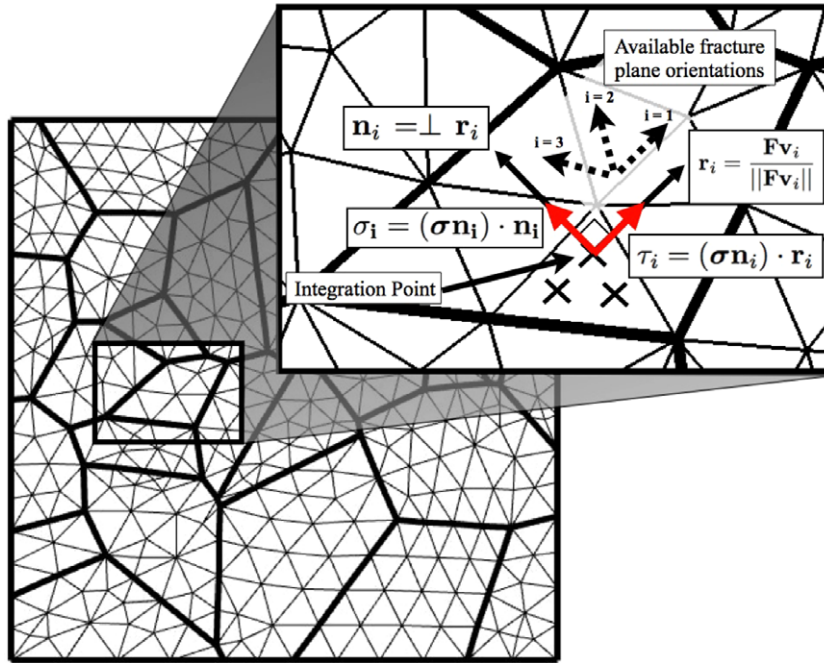


Fig. 2. Thirty-grain microstructural schematic depicting how the transgranular cracks are inserted.

Note that σ_i and τ_i are scalar quantities.

Once the algorithm determines that $\sigma_i \geq \sigma_{\text{crit}}$ or $\tau_i \geq \tau_{\text{crit}}$ at a given integration point, remeshing is accomplished by extending a line vector from both left and right sides of the integration point coordinate along the orientation until the line vector intersects the grain boundary. Note the assumption that cracks are straight across a grain. To support this assumption we cite the work of Li et al. [27] who conducted in situ single-crystal fracture experiments at room temperature using transmission electron microscopy (TEM) on Si_3N_4 and MgO ceramics. With atomic scale resolution, it was con-

cluded that in both ceramics, fracture surfaces were atomically flat or had a deviation of only a few atomic layers.

2.5. Boundary conditions

Virtual two-dimensional microstructures consisting of 30 and 200 grains were constructed using Voronoi tessellation. Typical microstructures are shown in Fig. 3. A plane strain assumption was used. At a given time, t , during the simulation the displacements of the top surface, d^{top} , are prescribed in the direction of \mathbf{X}_2 according to:

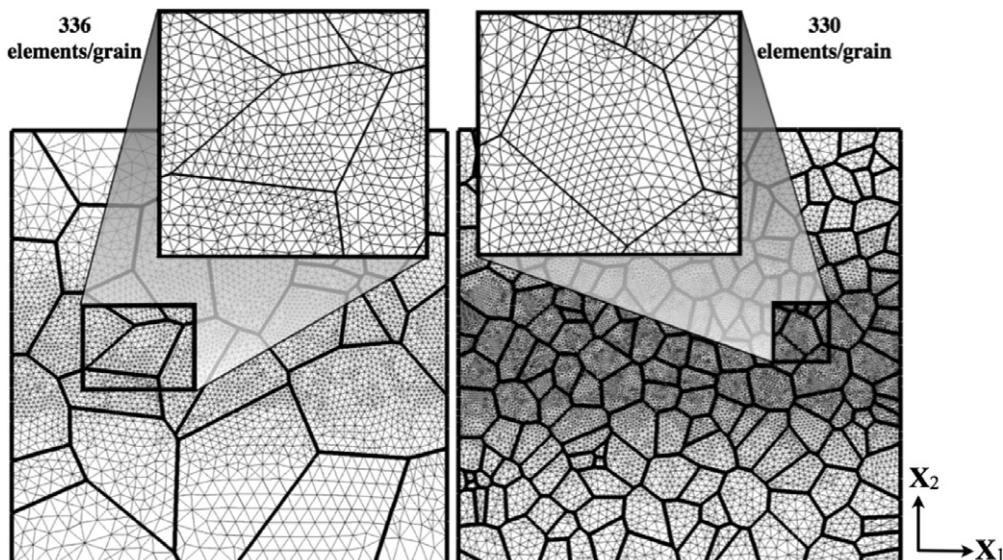


Fig. 3. Thirty- and 200-grain microstructures constructed using Voronoi tessellation.

$$d_2^{\text{top}}(t) = \frac{t}{t_{\text{tot}}} \epsilon_{\text{tot}} h \quad (18)$$

where t_{tot} is the total time of the simulation, ϵ_{tot} is the total strain and h is the specimen dimension. Therefore, the top surface velocity, v_2^{top} , and strain-rate are nominally constant (corresponding to the undeformed specimen dimension):

$$v_2^{\text{top}} = \frac{d_2^{\text{top}}(t)}{t} = \frac{\epsilon_{\text{tot}}}{t_{\text{tot}}} h = \dot{\epsilon} h \quad (19)$$

2.6. Constitutive laws

There are three different constitutive laws used within a simulation, one for the bulk material, one for the interfaces in the microstructure, or grain boundaries, and another for the transgranular cohesive interfaces dynamically inserted across grains.

Al_2O_3 was chosen as the material to model. The bulk response of the grains is assumed to be isotropic and linear elastic. In reality the elastic anisotropy of Al_2O_3 is equal to 1.2 [28]. However, in simulations conducted by Warner and Molinari [17], neglecting anisotropy did not substantially affect the mesoscopic failure. The parameters used include Young's modulus $E = 386 \text{ GPa}$, density $\rho = 3960 \text{ kg m}^{-3}$, and Poisson's ratio $\nu = 0.22$ [29].

The cohesive laws are characterized by the cohesive energy, G_c . These values characterize the grain boundary fracture properties and should be obtained from rigorous experimental tests. The experimental work of Yasuda et al. [24] suggests a uniform distribution of G_c between 1 and 22 J m^{-2} for the grain boundaries in Al_2O_3 . In addition to using a uniform distribution, we also investigate

normal, constant and bimodal distributions, all with the same mean value of $G_c = 11.5 \text{ J m}^{-2}$. The probability density functions for each of these distributions are shown in Fig. 4. The selection of the different distributions is under the assumption that as processing techniques advance, our ability to control defect distributions may also increase. In any case, the use of a distribution at the grain boundaries creates a more realistic description of the microstructure and may be needed to adequately capture the stochasticity of the physics of microfracture of brittle failure [19,30,31].

Cohesive properties are also needed for the transgranular interfaces. As Fang et al. [13] summarizes, past research on single-crystal alumina, indicates that a favorable crack path is most likely the rhombohedral cleavage **R** plane (with index $10\bar{1}2$) at room temperature. Wiederhorn [32] reports the fracture surface energy of the **R** plane as 6.0 J m^{-2} . This value was used for G_c for all microcracks nucleated in the grains. It should be noted that the cleavage fracture strength in Sapphire ($\alpha\text{-Al}_2\text{O}_3$) is anisotropic and can depend on the orientation and processing of test samples. For example, Becher [33] reports bend strengths in the range 275–826 MPa; however, for this initial study strength anisotropy is not included and σ_c was chosen as 600 MPa. This value was used for the dynamic insertion criterion of cohesive interfaces through grains, i.e. $\sigma_{\text{crit}} = \tau_{\text{crit}} = 600 \text{ MPa}$.

When using the cohesive interface approach there are length and time scales associated with the opening of a crack. The length of the process zone ahead of a stationary crack is estimated as [34–36]:

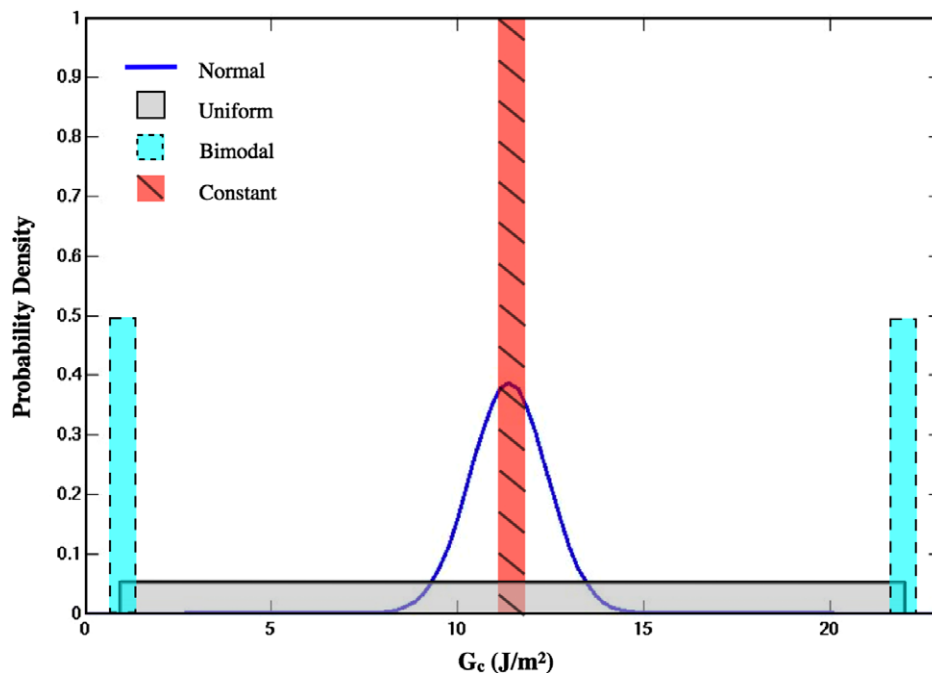


Fig. 4. Probability densities of critical energy release rate, G_c for four different distributions.

$$l_z = \frac{9\pi}{32} \frac{E}{1-\nu^2} \frac{G_c}{\sigma_c^2} \quad (20)$$

which is a material property that should be resolved by the finite-element discretization. This criterion is difficult to achieve on all grain boundaries in a computational microstructure while keeping the computational cost minimal. However, by choosing the process zone length, distributions of σ_c and δ_c result, and on average, adequate resolution of the process zone is satisfied. For example, in a 30-grain microstructure, $l_z = 6.4 \mu\text{m}$, the characteristic element length is $1.5 \mu\text{m}$, and the mean grain boundary length is $17.6 \mu\text{m}$ (for a mean grain size of $25 \mu\text{m}$). Thus, on average, there are 3–5 elements per cohesive zone length, varying according to the grain boundary length.

A grain size of $25 \mu\text{m}$ is chosen because past work indicates an increased tendency for cleavage fracture above submicron lengths [1,14,37]. In addition, the material processing of larger grain sizes, in the range of tens of microns, are capable of reaching greater theoretical densities, since defects such as pores and grain boundary impurities can be eliminated during the processing, again aligning more with simulations conducted here.

3. Results and discussion

3.1. Mesh convergence

The insertion criterion for transgranular fracture is based on the spatial location of integration points, therefore this method will always have some degree of mesh dependence. However, by using a fine enough mesh, a converged solution of crack path through the microstructure that did not change significantly according to the mesh density was obtained. The convergence analysis was conducted on a 30-grain microstructure, characterized by a mesh density parameter, ρ_m , defined as the average number of elements per grain. This mesh density parameter was devised because other measures, such as elements per area, will change if the grain size or specimen size is changed. To determine the relative differences between fracture paths obtained from different meshes, two-dimensional digital images of post-failure morphologies were compared using the open source software suite ImageMagick® [38]. The metric of difference considered was the average error over all pixels, referred to as the mean absolute error (MAE) expressed as a decibel value. A lower value of the MAE between two images indicates more similarity.

Fig. 5a shows zoom figures of four different mesh densities. Meshes 1, 2, 3, and 4 corresponding to $\rho_m = 6.5, 75.2, 572.0$, and 965.2 elements/grain, respectively. The highest mesh density investigated was controlled by current computational resources available. Fig. 5b shows fracture morphologies after failure for meshes 1, 2, 3, and 4. Note that the fracture surfaces obtained for meshes 3 and 4 are identical. Also shown in Fig. 5b is the MAE plotted in terms of

the mesh density. Higher mesh densities lead to a reproducible fracture morphology.

This leads to the conclusion that microstructures need high densities of elements to adequately resolve the transgranular fracture process. At the same time, more elements lead to unacceptably higher computation cost. One attempt to solve the problem was to use a graded mesh density, where more elements were concentrated near the middle of the specimen where fracture was assumed to localize, as shown in Fig. 3.

3.2. Interpreting computational results

It is instructive to concentrate on a single computational result to help understand the failure process as it evolves. To help quantify the evolution of the failure process, estimates of mesoscopic fracture toughness and percentages of transgranular fracture are determined. The estimate of mesoscopic fracture toughness is based on the idea of Griffith [39], i.e. fracture can be characterized by the conversion of elastic strain energy into surface energy. In our computations new surface area can easily be kept track of as it is created. The mesoscopic fracture energy release rate, G^m , is calculated using this idea.

$$G^m = \sum_{i=0}^{\text{Fracture surfaces}} \frac{G_c^{(i)} \times l^{(i)}}{L} \quad (21)$$

where $l^{(i)}$ is the fracture surface length with a corresponding $G_c^{(i)}$, and L is the sample width. Note that this does not represent the critical energy release rate, thus no subscript “c” is included. An estimate of the mesoscopic critical energy release rate, G_c^m , can be estimated after total failure has occurred and the specimen cannot support any load. Fig. 6a shows results obtained from a typical computation. Stress vs. strain is plotted along with the evolution of mesoscopic fracture energy and per cent transgranular fracture. Shown in Fig. 6b are the corresponding stress contours (sub-plots 1–11) for the data points shown in Fig. 6a. A pre-crack is imposed in the specimen to begin crack growth in the center of the specimen where the mesh is fine enough to adequately resolve the cohesive zones. The three available crack path orientations of each grain are also shown in Fig. 6b, sub-plot #1.

The stress begins to load elastically but deviates quickly from linearity due to the pre-crack. As loading continues, a stress concentration forms at the tip of the pre-crack (sub-plot #1) which nucleates a transgranular crack in the adjacent grain at the triple junction, which begins to propagate (as shown in sub-plots 2–4). During this time, the percentage of transgranular fracture and the mesoscopic fracture energy begins to grow. Recall that the percentage of transgranular fracture is based on the fracture surface area (or length, since simulations are plane strain).

It is interesting to note the change in stress contours and crack evolution as the primary crack propagates across the specimen. Examining sub-plots 5–7, the stress ahead of the

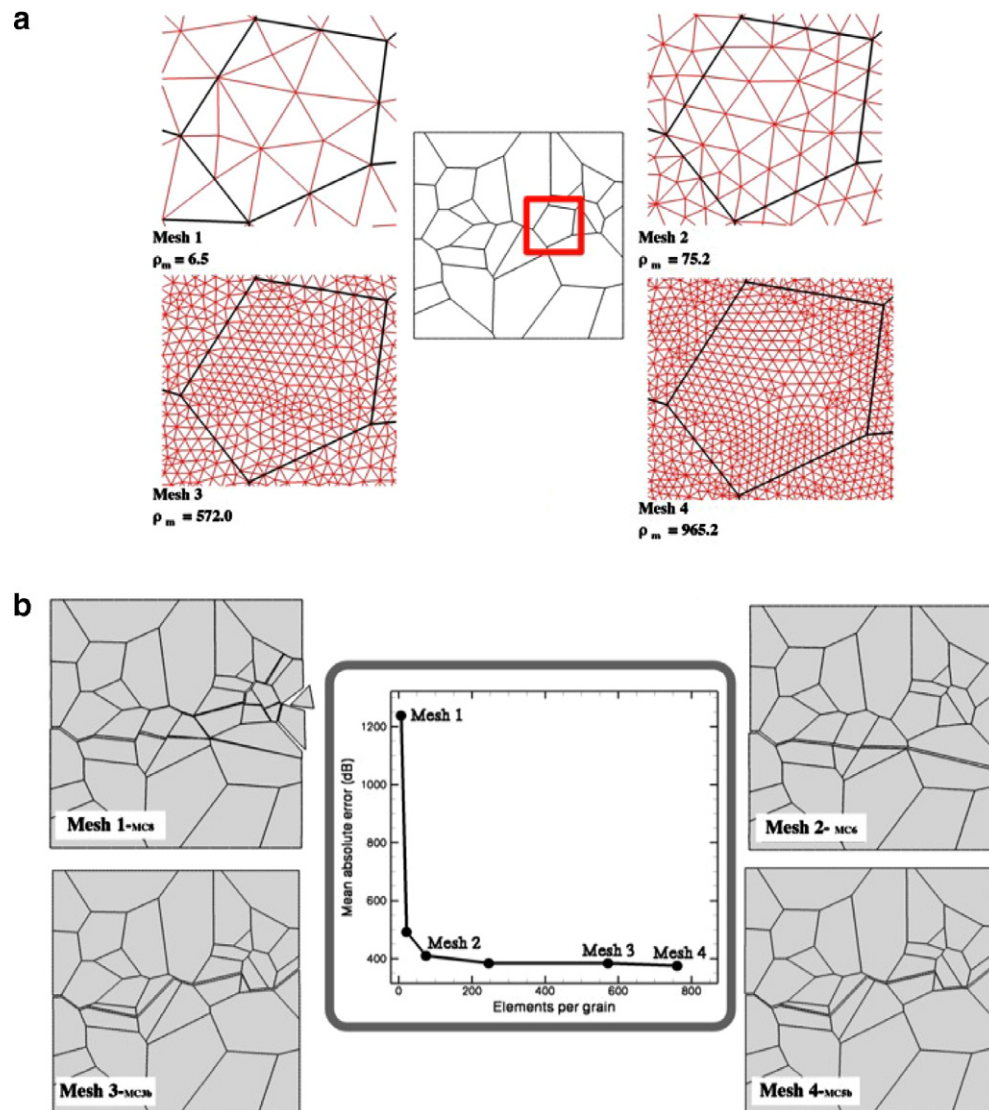


Fig. 5. (a) Thirty-grain microstructure used in convergence studies, along with an enlargement of microstructures with different mesh densities. Meshes 1, 2, 3, and 4 correspond to $\rho_m = 6.5, 75.2, 572.0$, and 965.2 elements/grain, respectively. (b) Fracture morphologies after failure for meshes 1, 2, 3, and 4. Note that the fracture surface obtained for meshes 3 and 4 are identical. Also shown is the mean absolute error plotted in terms of the mesh density. Higher mesh densities lead to a reproducible fracture morphology.

crack tip becomes uniformly high throughout the remaining load-bearing section. This leads to the nucleation of many microcracks ahead of the primary crack that produces crack branching. This effect may be controlled by imposing a much lower strain-rate or by using a larger representative volume element (which will only delay the effect).

An estimate of the critical energy release rate is obtained from the steady-state value of the mesoscopic fracture energy after stress unloading has occurred. From Fig. 6a this value is approximately $G_c^m = 14.1 \text{ J m}^{-2}$. In addition, the morphology of fracture is about 70% transgranular.

3.3. Effect of grain boundary distribution

As an application of this modeling technique we examine the effect of four different grain boundary distributions

(i.e. uniform, normal, constant and bimodal) of G_c , all with that same mean value of $G_c = 11.5 \text{ J m}^{-2}$, on the overall response of Al_2O_3 . Displacement-controlled loading conditions were used at a strain-rate of $7.0 \times 10^4 \text{ s}^{-1}$. For each distribution, 20 simulations were conducted using 20 different microstructures consisting of 30 grains (to limit computational cost) that were generated randomly using Voronoi tessellation. The use of 20 different microstructures was an attempt to capture the stochastic nature of brittle failure. A pre-crack is inserted in each microstructure, each with approximately the same length. From the simulations, the mean and standard deviation of fracture strength, mesoscopic fracture toughness and percentage of transgranular fracture are calculated as shown in Fig. 7. Results are ranked according to fracture strength, left to right. Note that the error bars represent standard deviations. A number of observations are worth noting.

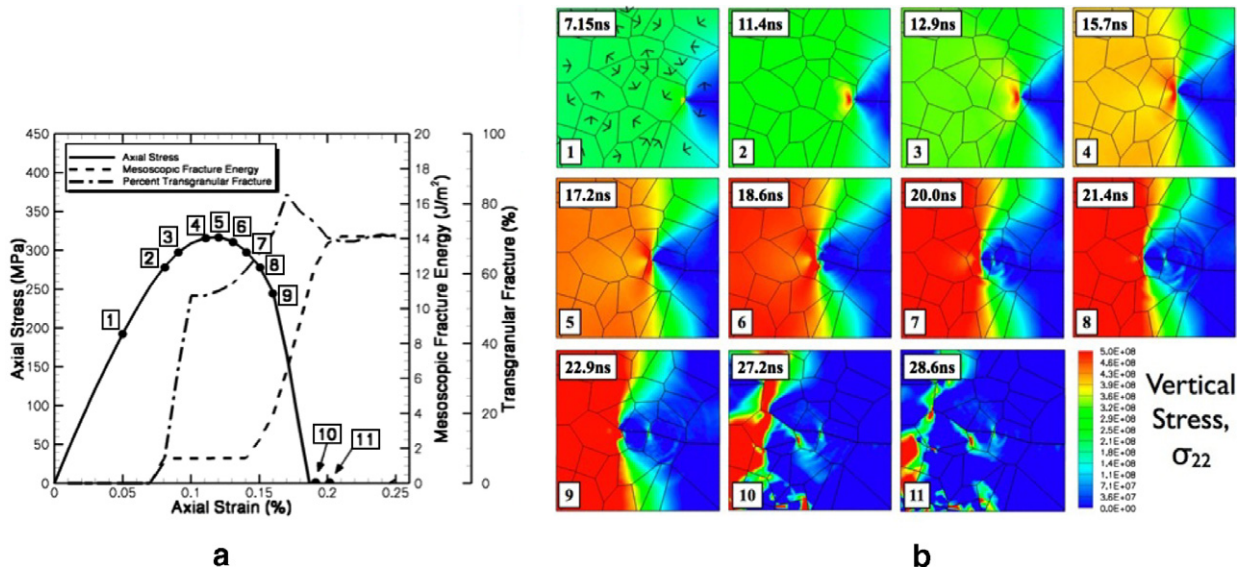


Fig. 6. Typical simulation result showing (a) axial stress in terms of axial strain plotted along with the evolution of mesoscopic fracture energy and per cent transgranular fracture, and (b) stress contours show the crack path as it propagates across the specimen. Each subfigure in (b) is numbered corresponding to a point on the curve in (a).

The ranking from strongest to weakest is normal, constant, uniform and then bimodal, although the mean strengths of the normal, constant and uniform distributions overlap statistically. The variability in fracture strength, denoted by the error bars, is greater when the strength is higher. Accordingly, the variability associated with the bimodal distribution, which is observed to have the lowest fracture strength, is low. The results for a normal and constant distribution are very similar. This is

believed to be an artifact of the relatively small representative volume element used and of the narrow normal distribution. Since there is a limited number of grain boundaries for 30-grain microstructures, these distributions “look” very similar to the propagating crack. Had there been more grains in the microstructure, perhaps these results would have a more pronounced difference with a weaker strength for the normal distribution. Relatively high percentages of transgranular fracture for the normal and constant distributions are a result of the small number of weak grain boundaries available for crack propagation. This observation agrees with the weakest link theory of brittle ceramics [40–42].

The uniform distribution results in approximately 17% lower fracture strength as compared to the normal distribution with 40% less transgranular fracture. However, there is only an 6% difference in the mean values of mesoscopic fracture toughness between the normal and uniform distributions. This is an interesting observation because the percentages of transgranular fracture are quite different. For the normal distribution, cracks tend to propagate in a planar path, with little deviation until crack branching occurs. This is in contrast to the uniform distribution which has an increased number of weak grain boundaries for the crack to travel along. Indeed, by examining simulation results, it is observed that the crack travels a much more tortuous path around grains, on a grain boundary with a smaller value of G_c . While the crack path is more tortuous for the uniform distribution (as compared to the normal distribution), no sufficient gain of fracture toughness is observed. This highlights the relationship between grain boundary-to-grain toughness ratio (E_{GB}/E_G) and may help to explain the experimental differences observed in the works of Gutshall and Gross [1] and

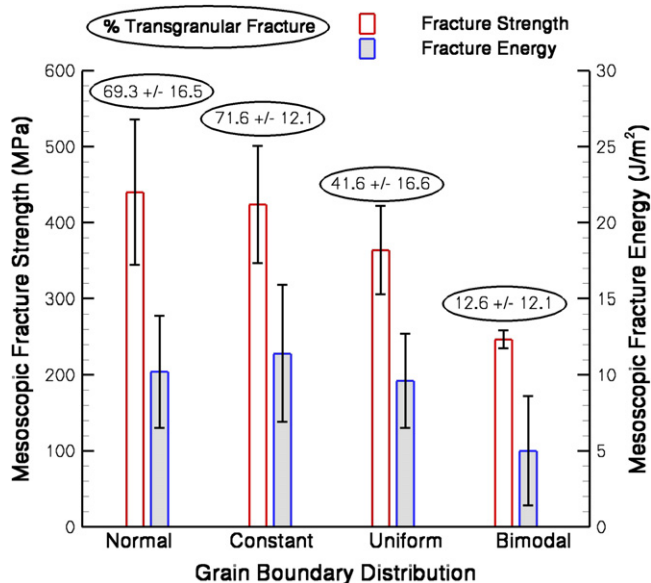


Fig. 7. Estimates of mesoscopic fracture strength and energy for various grain boundary distributions of G_c using displacement-controlled loading. Values enclosed by ellipses above each distribution indicate the percentage of transgranular fracture. Note that values are based on 20 different simulations, each with a different microstructure.

Simpson [6]. This result also seems to confirm the hypothesis stated in Section 1, i.e. that a tortuous crack path may not always lead to increased meso- or macroscopic energy dissipated in the failure process; ultimately it depends on the microscopic energy dissipation mechanisms and how they interact.

The mean values of the bimodal distribution, as compared to the normal distribution, yielded 44% and 51% lower fracture strength and mesoscopic fracture energy, respectively. On average, 12.6% of the fracture morphology was transgranular cracking. In most cases, a crack was able to “find” a weak grain boundary to propagate along. Perhaps the only noteworthy characteristic of this result is the relatively small variation associated with the fracture strength, a desirable trait in the design of engineering components.

3.4. Effect of grain geometry

The ability to tailor a microstructure for desired performance is believed to play a crucial role in next-generation materials. Taking a microstructural engineering approach, the performance of the uniform distribution microstructure was improved. As mentioned earlier, this distribution is observed in experimental work [24]. Observations of crack path for the uniform distribution discussed previously suggest that one possible route to improving toughness would be elongation of the grain geometry with respect to the loading axis, promoting an increased length of travel for a crack propagating along a weak grain boundary. Elongation of the grains was estimated by assuming the grains were elliptical in shape. The average eccentricity, e (which characterizes the elongation of an ellipse, $0 \leq e < 1$), for the 20 different microstructures used earlier ranged from 0.4 to 0.6. Two additional simulations were conducted with $e = 0.79$ and 0.90.

In both cases, failure strength and mesoscopic fracture energy increased. The case of $e = 0.79$ yielded a 12.9% and 37.5% increase in mesoscopic failure strength and fracture energy, respectively; 63.5% of the fracture surface was transgranular. Similarly for $e = 0.90$, a 29.7% and 140.6% increase in mesoscopic failure strength and fracture energy were obtained, respectively, with 61.8% transgranular fracture.

While mechanical performance was increased, the desired crack path was not achieved. Fracture morphologies indicate that instead of increased propagation on longer, weak grain boundaries, cracks chose a path through the grains. The reason for this is that elongation of the microstructure increases the number of grain boundaries aligned with respect to the loading axis (vertically). This direction is less prone to crack propagation because the resolved stress on the vertical grain boundaries is relatively low, and the ratio of fracture energy E_{GB}/E_G is such that transgranular fracture is energetically favorable, indicated by the increase in per cent transgranular fracture obtained, compared with unmodified microstructures.

Had the bulk grain toughness been higher, perhaps vertical crack climb may be observed.

This illustrates the difficulty of grain boundary engineering (and the need for computational materials design), i.e. while trying to promote one mechanism, one may also initiate a completely different mechanism. For example, the elimination of grain boundaries prone to fracture promotes toughening mechanisms ahead of the primary crack. As shown in Fig. 8, discontinuous crack propagation occurs as a result of “daughter” cracks that initiate ahead of the primary “mother” crack. Toughening is a result of the elastic ligaments bridging the cracks. This toughening mechanism has been experimentally observed in polycrystalline alumina [43].

Another possible avenue for exploring computational materials design using mesoscopic simulations is to examine the effects of grain size distribution on the overall mechanical response. From a materials point of view this is very attractive; however, computationally there are severe limitations to completing such work. For example, when using the cohesive interface approach, the cohesive zone length should be small compared to the grain boundary lengths. In fact, the computational microstructures used throughout this investigation have a range of grain

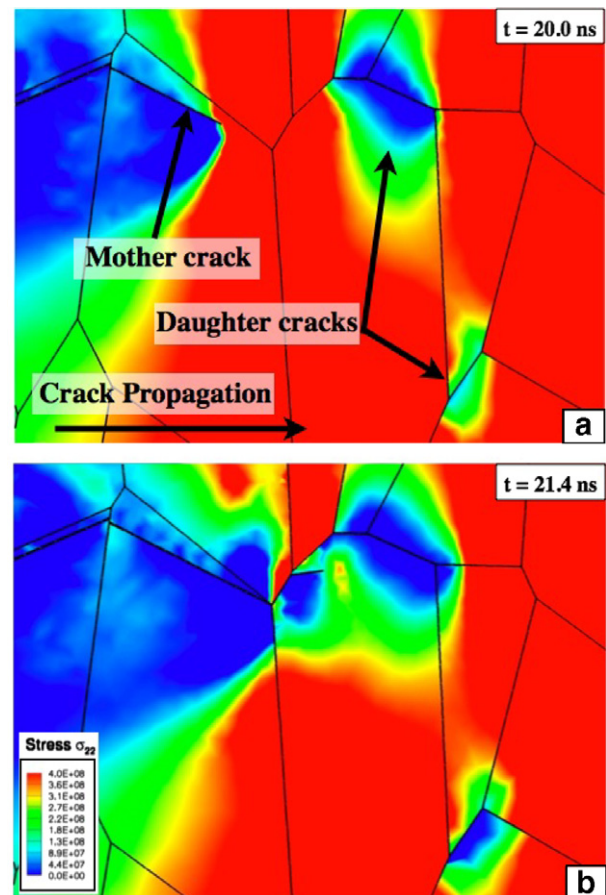


Fig. 8. Contours of the stress in the vertical direction, aligned with the loading axis of the complex crack path for a microstructure with a uniform distribution of G_c and elongated grains with respect to the loading axis.

boundary lengths, thus, we expect the microstructures to be adequately resolved in the case of longer grain boundaries, but not for shorter ones. Therefore, fracture along some grain boundaries may be controlled by the cohesive strength and therefore is not toughness driven (as we expect for brittle fracture). The interaction of cohesive zones with the geometry of the grains raises the important question of fracture remaining a toughness-driven process. We acknowledge this concern; this is currently a limitation with finite-element-based fracture micromechanics and limits our ability to examine grain size distributions within the current framework.

3.5. Effect of the RVE

In order to validate the 30-grain simulations results, a 200-grain simulation with a uniform distribution loaded at the same rate of deformation was conducted. Due to the computational expense, only one microstructure was considered. In terms of failure strength, the results are encouraging. A mesoscopic failure strength of 353 MPa was obtained, which lies within the statistical variation of the strength results obtained for 30-grain microstructures. However, a mesoscopic fracture energy of 21.2 J m^{-2} resulted, over double the mean value of the 30-grain samples. The RVE size effect on fracture energy indicates the full microcrack process zone is not fully refined and may be affected by the different ligament sizes between pre-crack and the sample edge. Bazant [44] reviews various experimental studies where a size dependence was observed. Thus, while only an approximation, the mesoscopic fracture energy parameter characterizes qualitatively the surface energy associated with the formation of the process zone in brittle materials. Further research, development and computational resources are needed to attain realistic size-independent fracture toughness through simulations.

4. Summary

A new technique to model transgranular fracture has been developed to study the mesoscopic response of Al_2O_3 under tensile loading. The following conclusions are made.

- The technique is a computational tool that uses dynamic insertion of cohesive interfaces to model intergranular and transgranular fracture. Convergence of the fracture morphology across sample is obtained and simulations are able to capture the mesoscopic failure strength, the evolution of mesoscopic fracture energy qualitatively and percentages of transgranular fracture.
- Statistics on mesoscopic failure strength and fracture energy are obtained using 20 different microstructures in an attempt to capture the stochastic nature of brittle materials. In addition, four different grain boundary distributions are examined and are ranked according to decreasing failure strength, i.e. normal, constant, uni-

form, then bimodal (while the variation in strength for normal and constant distribution overlap statistically). Statistical variation increased with increasing strength.

- Microstructures with a uniform distribution seem the best candidate for microstructural engineering through modifying grain geometry. While significant enhancements were made by creating elongated grained microstructure, the desired engineering crack path was not observed due to adversely placed grain boundaries and the ratio of the grain boundary fracture energy to the bulk grain fracture energy. However, interesting fracture micromechanisms were revealed, and simulations seem promising in regard to a first step analysis in grain boundary engineering.

Acknowledgements

The support of the Army Research Office under the Grant No. W911NF-05-1-0370 is gratefully acknowledged as well as the support of the Army Research Laboratory through a subcontract from the University of Nebraska-Lincoln under the Grant No. 25-1105-0005-200. R.H.K. is grateful to Derek Warner for fruitful discussions leading to this work.

References

- [1] Gutshall PL, Gross GE. *Eng Fracture Mech* 1969;1:463–71.
- [2] Yang WJ, Yu CT, Koboyashi AS. *J Am Ceramic Soc* 1991;74(2):290–5.
- [3] Swab JJ, Quinn GD. *J Am Ceramic Soc* 1998;81(9):2261–8.
- [4] Evans AG. *J Am Ceramic Soc* 1990;73(2):187–206.
- [5] Becher PF. *J Am Ceramic Soc* 1991;74(2):255–69.
- [6] Simpson LA. *J Am Ceramic Soc* 1973;56(1):7–11.
- [7] Lin T, Evans AG, Ritchie RO. *J Mech Phys Solids* 1986;34(5):477–97.
- [8] Zhang XZ, Knott JF. *Acta Mater* 2000;48:2135–46.
- [9] Smith GE, Crocker AG, Flewitt PEJ, Moskvic R. *Mater Sci Technol* 2002;18(November):1329–34.
- [10] Smith GE, Crocker AG, Moskvic R, Flewitt PEJ. *Philos Mag A* 2002;82(17/18):3443–53.
- [11] Crocker AG, Flewitt PEJ, Smith GE. *Int Mater Rev* 2005;50(2):99–124.
- [12] Fang Y, Ravi-Chandar K, White K. *J Am Ceramic Soc* 2002;85(7):1783–7.
- [13] Fang Y, Fossier T, White K. *Scr Mater* 2004;50:127–30.
- [14] Galal Yousef S, Rödel J, Fuller Jr ER, Zimmermann A, El-Dasher BS. *J Am Ceramic Soc* 2005;88(10):2809–16.
- [15] Espinosa HD, Zavattieri PD, Dwivedi SK. *J Mech Phys Solids* 1998;46(10):1909–42.
- [16] Sukumar N, Srolovitz DJ, Baker TJ, Prevost J-H. *Int J Numerical Methods Eng* 2003;56:2015–37.
- [17] Warner DH, Molinari JF. *Acta Mater* 2006;54:5135–45.
- [18] Nittur PG, Maiti S, Geubelle PH. *J Mech Phys Solids* 2007;56(3):993–1017.
- [19] Kraft RH, Molinari JF, Ramesh KT, Warner DH. *J Mech Phys Solids* 2008;56:2618–41.
- [20] Belytschko T, Liu WK, Moran B. *Nonlinear finite elements for continua and structures*. John Wiley & Sons Ltd.; 2000.
- [21] Taylor L, Flanagan D. Pronto2d: a two-dimensional transient solid dynamics program, Technical Report SAND86-0594, Sandia National Laboratories, 1987.
- [22] Barenblatt GI. In: Dryden HL, von Karman T, editors. *Advances in applied mechanics*. New York: Academic Press; 1962.
- [23] Dugdale DS. *J Mech Phys Solids* 1960;8:100–4.

- [24] Yasuda K, Tatami J, Harada T, Matsuo Y. *Key Eng Mater* 1999;2:573–6.
- [25] Streitz FH, Mintmire JW. *Phys Rev B* 1994;50(16):11996–2003.
- [26] Zhou XW, Wadley HNG, Filhol J-S, Neurock NN. *Phys Rev B* 2004;69(035402).
- [27] Li S, Iwamoto C, Matsunaga K, Yamamoto T, Ikuhara Y. *Appl Surf Sci* 2005;241:68–74.
- [28] Rice RW. *J Mater Sci Lett* 1994;13:1261–6.
- [29] Wereszczak AA, Swab JJ, Kraft RH. Effects of machining on the uniaxial and equibiaxial flexure strength of CAP3 AD-995 Al_2O_3 . Technical Report ARL-TR-3617, Army Research Laboratory, 2005.
- [30] Jayatilaka ADeS, Trustrum K. *J Mater Sci* 1977;12:1426–30.
- [31] Espinosa HD, Zavattieri PD. *Acta Mater* 2001;49:4291–311.
- [32] Wiederhorn SM. *J Am Ceramic Soc* 1969;52(9):485–91.
- [33] Becher PF. *J Am Ceramic Soc* 1975;59(1–2):59–61.
- [34] Palmer AC, Rice JR. *Philos Trans R Soc Lond A* 1973;332: 527–48.
- [35] Rice JR. In: Dziewonski A, Boschi E, editors. *Physics of the earth's interior*. Amsterdam: North-Holland Publishing Company; 1980. p. 555.
- [36] Falk ML, Needleman A, Rice JR. A critical evaluation of cohesive zone models of dynamic fracture. *J Phys IV* (5th European Mechanics of Materials Conference in Delft, the Netherlands) 2001, Pr.5.43–Pr.5.50.
- [37] Muchtar A, Lin LC. *Acta Metallurgica* 1998;5:1683–90.
- [38] Thyssen A. Imagemagick v6 Examples – Image Comparing, July 2006. Available from: <http://www.imagemagick.org/Usage/compare/>.
- [39] Griffith AA. *Philos Trans R Soc Lond A* 1921;221:163–98.
- [40] Weibull W. *Ingenioersvetenskapsakad* 1939;139:45.
- [41] Weibull W. *Ingenioersvetenskapsakad* 1939;153:55.
- [42] Petrovic JJ. *Metallurgical Mater Trans A* 1987;18(11):1829–34.
- [43] Kruzic JJ, Cannon RM, Ritchie RO. *J Am Ceramics Soc* 2004;87(1):93–103.
- [44] Bazant ZP. In: Bazant ZP, editor. *Fracture Mechanics of concrete structures*. Elsevier Applied Science; 1992. p. 68–103 [chapter 6].